Computers and Electronics in Agriculture 242 (2026) 111350

Contents lists available at ScienceDirect

Computers and Electronics in Agriculture

journal homepage: www.elsevier.com/locate/compag

GNSS/MEMS INS tightly coupled algorithm for agricultural machinery navigation enhanced by random forest-based behavioral state awareness

Yihang Feng [a,b,e,f], Guanwen Huang [a,b,c], Mingfeng Wang [f,*], Xin Li [a,b,c], Zhenhong Li [a,b,d], Hang Li [b], Kai Zhang [b], Ce Jing [b]

[a] State Key Laboratory of Loess Science, Chang'an University, Xi'an 710054, China
[b] College of Geological Engineering and Geomatics, Chang'an University, Xi'an 710054, China
[c] Key Laboratory of Ecological Geology and Disaster Prevention, Ministry of Natural Resources, Xi'an 710054, China
[d] Key Laboratory of Western China's Mineral Resource and Geological Engineering, Ministry of Education, Xi'an 710054, China
[e] Big Data Center for Geosciences and Satellites, Chang'an University, Xi'an 710054, China
[f] Department of Mechanical and Aerospace Engineering, Brunel University of London, London, UB8 3PH, UK

ARTICLE INFO

Keywords:
GNSS
MEMS INS
Random forest
Butterworth filter
Non-holonomic constraints

ABSTRACT

Global navigation satellite system (GNSS)/micro-electro-mechanical systems inertial navigation system (MEMS INS) algorithm is widely used in agricultural machinery navigation. However, several issues remain noteworthy, uneven terrain induces more high-frequency noise than other environments, which severely affects the accuracy of MEMS INS. In addition, occlusion environment, such as field windbreak, degrades GNSS signal quality. Although Butterworth filter and non-holonomic constraints (NHC) have been validated as effective solutions for these issues, which still face the following limitations in agricultural scenarios. This is because the power spectral density (PSD) of MEMS INS data exhibits distinct energy distribution among different states, therefore it is unreasonable to apply uniform cutoff frequency same as classic Butterworth filter. Additionally, jumping and slipping frequently occur, which can invalidate the zero-velocity assumption of NHC. Therefore, given the limitations of previous studies, this paper proposes a random forest (RF)-based model to identify machinery states and predict body-frame (right and up) velocities. Then, adaptive cutoff frequencies are selected for the Butterworth filter. Furthermore, the measurement and stochastic models of NHC are optimized by states and body-frame velocities. Experiments show that the proposed algorithm can achieve centimeter-level positioning accuracy and the heading angle error of only 0.33°.

1. Introduction

With the growth of population, agricultural modernization has become increasingly important while high-precision navigation systems are essential to achieve this target (Li et al., 2021a). Currently, commonly used navigation systems include Global Navigation Satellite Systems (GNSS), Inertial Navigation Systems (INS), LiDAR navigation systems, vision navigation systems, and combination in between them (Xie et al., 2023). However, LiDAR- and vision-based navigation systems are less preferrable in agricultural machinery navigation, due to either high cost (Lü et al., 2018; Jiang and Ahamed, 2025), or sensitivity to lighting conditions (Lü et al., 2022).

GNSS, thanks to its real-time capability, has been widely adopted in many areas (Li et al., 2021b, c; Lai et al., 2025). Enhanced by the Real-Time Kinematic (RTK) and Precise Point Positioning (PPP) techniques, the positioning accuracy can normally achieve centimeter-level in ideal conditions (Cui et al., 2025; Huang et al., 2023; Wang et al., 2023). However, it dramatically decreases in obstructed agricultural environments (Guo et al., 2018). On the other hand, INS is an independent navigation system with high short-term accuracy, although its errors accumulate over time. Therefore, integrating INS with GNSS can potentially establish a robust navigation system and become a popular solution in agricultural applications (Feng et al., 2023; Huang et al., 2022).

Due to the lower price and the smaller size than high-precise INS (Sun et al., 2022), micro-electro-mechanical systems (MEMS) INS is widely used in many areas despite its higher error accumulation rate (Rafatnia et al., 2019). Consequently, research has focused on advanced

* Corresponding author.
E-mail address: Mingfeng.Wang@brunel.ac.uk (M. Wang).

https://doi.org/10.1016/j.compag.2025.111350
Received 22 August 2025; Received in revised form 9 December 2025; Accepted 16 December 2025
Available online 22 December 2025

algorithms to overcome the limitations of the hardware. For example, dual-antenna GNSS/MEMS INS integration can achieve centimeter-level positioning accuracy and heading accuracy within 1 ° (Zhang et al., 2015; Zhang et al., 2021). Notably, those are all based on the loosely coupled (LC) algorithms and the robustness is still questionable. The tightly coupled (TC) algorithms can offer superior robustness, thanks to directly integrating raw observations measurements of GNSS with INS (Niu et al., 2016). However, they still face limitations in complex agricultural scenarios, which are mainly from the following two aspects:

On the one hand, because irregular field topography is a high-vibration environment, MEMS INS exhibits considerable high-frequency noise, which must be removed. To reduce the influence, time-domain high-frequency noise removal algorithms were employed, however the effectiveness of these algorithms is limited (Rohac et al., 2011). Therefore, researchers have applied frequency-domain based low-pass filtering algorithm, such as Wavelet de-noising (Wu and Yang, 2007; Xu et al., 2018) and Butterworth (Hu et al., 2020a). The wavelet de-noising algorithm has low computational efficiency. Classic Butterworth has higher computational efficiency; however, this method does not distinguish different vehicle behavioral states. In vehicle navigation, due to smooth road surfaces and uniform states, the power spectral density (PSD) of INS data exhibits similar energy distribution patterns across different states. Therefore, setting a uniform cutoff frequency without distinguishing states is reasonable. However, it has limitations in agricultural machinery navigation, where uneven field surfaces and unique motion states cause significant variations in PSD energy distribution across frequency bands under different states. For instance, when agricultural machinery operates on bumpy terrain, genuine high-frequency changes occur in angular velocity and velocity, resulting in noticeably higher energy distribution in mid-frequency ranges. In this case, applying a low cutoff frequency would filter out these real motion signals, leading to distorted navigation results. Hence, accurate recognition of machinery behavioral states is crucial to overcoming this limitation.

On the other hand, non-holonomic constraints (NHC) assume that right and up velocities are near zero, meaning the vehicle rarely jumps and slips (Niu et al., 2007). NHC is widely used in vehicle navigation, especially where GNSS signals are weak, such as urban canyons and tunnels (Sun et al., 2020; Wang et al., 2022; Jing et al., 2025). Some studies suggest using different neural networks to predict velocities for straight driving and turning, since slipping is more likely during turns (Li et al., 2023). The influence of varying behavioral states on NHC is even more critical in agricultural machinery navigation due to soft soil and uneven terrain, which increases the probability of jumping and slipping during turns and bumps. In summary, the assumptions underlying NHC present significant limitations in agricultural navigation, and the key to overcoming these limitations lies in accurate prediction of machinery behavioral states and velocities.

Based on the above discussion, if the behavioral states and velocities of agricultural machinery can be accurately predicted, both Butterworth filtering and NHC can be optimized. Currently, in the field of vehicle navigation, extensive research has been conducted on identifying states using INS data (Gao and Zhao, 2016). However, in the agricultural domain, INS-based behavioral state recognition studies have mainly focused on livestock (Rahman et al., 2018; Peng et al., 2020; Kirsch et al., 2025), with limited research on agricultural machinery behavior recognition. Existing animal behavior recognition algorithms commonly employ complex machine learning methods such as Long Short-Term Memory (LSTM) networks and Convolutional Neural Networks (CNN), which, despite their high accuracy, suffer from poor real-time performance (Li et al., 2024). Compared to the above-mentioned algorithms, some machine learning methods, such as Support Vector Machines (SVM), Decision Trees and Random Forests (RF), offer higher computational efficiency. Especially, RF is an ensemble classifier, which can achieve high accuracy and robustness without complex data preprocessing, which has attracted extensive attention from researchers (Zhou et al., 2023). Moreover, RF can also construct regression trees, enabling not only the recognition of behavioral states but also accurate prediction of body-frame velocities. These advantages make RF particularly well-suited for agricultural machinery navigation scenarios.

Selecting a suitable data fusion algorithm is also a crucial step. The GNSS/MEMS INS tightly coupled (TC) integration algorithm represents a typical nonlinear system, and existing data fusion methods for such models can generally be categorized into two groups: 1) Lie group/Lie algebra-based filtering methods. For example, Hu et al. (2025) applied this approach to strapdown inertial navigation system (SINS)/Doppler velocity log (DVL) TC integration, and demonstrated that the method is immune to the initial attitude error and offers advantages in both convergence speed and steady-state accuracy. 2) Kalman filter variants, including the extended Kalman filter (EKF), unscented Kalman filter (UKF), and cubature Kalman filter (CKF) (Gao et al., 2020). Gao et al. (2023a) realized INS/CNS/SRS TC integration based on EKF and improved the filtering accuracy by incorporating a chi-square test-based covariance estimation method. To address the linearization errors of EKF, Hu et al. (2019) proposed a robust UKF and applied it to GNSS/INS TC integration. Considering the high computational burden of UKF, Hu et al. (2015a; 2015b) introduced a derivative UKF to improve efficiency. Further studies have developed a variety of improved UKF algorithms (Gao et al., 2015, 2017, Hu et al., 2015c, 2018, 2020b, c; Yang et al., 2016) to enhance adaptability and robustness against uncertainties in kinematic and measurement models. Meanwhile, Hu et al. (2023) established a decentralized multi-sensor information fusion framework based on robust UKF, achieving INS/GNSS/CNS integration. In terms of CKF, Gao et al. (2023b) proposed a closed-loop covariance feedback-based INS/GNSS TC integration method, and further developed a cubature rule-based distributed optimal fusion algorithm for MIMU/GNSS/CNS integration (Gao et al., 2021a, b). Other improved CKF methods mainly focus on optimizing noise statistics and enhancing robustness (Gao et al., 2021a, b, 2022; Hu et al., 2024; Zhang et al., 2019). Although extensive research has been conducted on Lie group methods, UKF, and CKF, most of these studies target high-dynamic platforms such as UAVs and hypersonic vehicles, and the algorithms often involve higher computational complexity. Therefore, in this work, EKF is selected as the data fusion algorithm, considering both computational efficiency and engineering applicability.

In this paper, RF-based GNSS/MEMS INS TC algorithm is proposed to optimize both the Butterworth filtering and NHC models, as well as to enhance accuracy and robustness in agricultural machinery navigation. The contribution of the proposed algorithm are as follows: 1) A RF model is employed to predict both the behavioral states and the body-frame velocities; 2) The influence of behavioral states on the PSD energy distribution of INS data is fully considered, and a novel state-based Butterworth filtering strategy is designed to prevent signal distortion caused by excessive filtering; 3) To address the inaccuracy of the NHC model, the RF-predicted body-frame velocities are used to replace the zero velocity assumption. In addition, a measurement noise adjustment function is introduced, which is based on the behavioral states, to further optimize the stochastic model of the NHC.

The rest of the paper is organized as follows: Section 2 describes the proposed algorithm, including the framework, TC model, RF algorithm, and the optimized Butterworth and NHC methods. Section 3 presents experimental analysis and discussion. Section 4 concludes the paper.

2. Methods

In this section, a framework of the proposed GNSS/MEMS INS TC algorithm is illustrated, followed by detailed explanation of the TC model, RF algorithm, and the optimized Butterworth and NHC methods in the framework.

2.1. Framework

As shown in Fig. 1, there are four steps in the proposed framework: 1) *Training data Preparation*: this step includes two parts: (a) feature extraction from MEMS INS data, and (b) process high-precision Position and Orientation System (POS) data via IE Software® to generate labels, including body-frame velocities and behavioral states. 2) *RF models training*: use features and labels obtained in Step 1 to train the RF models and save them. 3) *Input Preparation*: prepare the input features through feature extraction. 4) *Butterworth and NHC Optimization*: use the behavioral states predicted by the RF model to optimize the Butterworth filter via decreasing the noise of MEMS INS data. Additionally, both the predicted states and body-frame velocities are utilized to refine the NHC model. Finally, all information is fused by an Extended Kalman Filter (EKF) to obtain the final navigation solution.

2.2. Tightly coupled (TC) model

2.2.1. System model

The tightly coupled state-space model of GNSS/INS can be written as (Feng et al., 2025):

$$\delta \boldsymbol{x} = \left[\delta \boldsymbol{\psi}^e_{eb} \ \delta \boldsymbol{v}^e_{eb} \ \delta \boldsymbol{r}^e_{eb} \ \delta \boldsymbol{b}_a \ \delta \boldsymbol{b}_g \ \Delta\nabla \boldsymbol{N}_{rb}\right] \tag{1}$$

where the superscript e represents Earth-centered and Earth-fixed (ECEF) frame, subscript b denotes body-frame, $\delta\boldsymbol{\psi}^e_{eb}$, $\delta\boldsymbol{v}^e_{eb}$, and $\delta\boldsymbol{r}^e_{eb}$ are attitude, velocity, and position errors, respectively. $\delta\boldsymbol{b}_a$ and $\delta\boldsymbol{b}_g$ are INS accelerometer and gyroscope biases, and $\Delta\nabla\boldsymbol{N}_{rb}$ is the double-difference ambiguities between the GNSS rover and base stations.

Then, the system model can be defined as (Zhang et al., 2017):

$$\begin{cases} \delta\dot{\boldsymbol{\psi}}^e_{eb} = -\boldsymbol{C}^e_b\delta\boldsymbol{b}_g - \left(\boldsymbol{\omega}^e_{ie}\times\right)\delta\boldsymbol{\psi}^e_{eb} + \boldsymbol{\xi}_\psi \\ \delta\dot{\boldsymbol{v}}^e_{eb} = \boldsymbol{C}^e_b\delta\boldsymbol{b}_a + \left((\boldsymbol{C}^e_b\boldsymbol{f}^b_{ib})\times\right)\delta\boldsymbol{\psi}^e_{eb} - \left(2\boldsymbol{\omega}^e_{ie}\times\right)\delta\boldsymbol{v}^e_{eb} + \boldsymbol{\xi}_v \\ \delta\dot{\boldsymbol{r}}^e_{eb} = \delta\boldsymbol{v}^e_{eb} + \boldsymbol{\xi}_r \\ \delta\dot{\boldsymbol{b}}_a = \boldsymbol{\xi}_{ba} \\ \delta\dot{\boldsymbol{b}}_g = \boldsymbol{\xi}_{bg} \\ \delta\Delta\nabla\dot{\boldsymbol{N}}_{rb} = \boldsymbol{\xi}_N \end{cases} \tag{2}$$

where the subscript i denote the inertial-frame, $\boldsymbol{C}^e_b$ is the attitude matrix relating the body-frame to the ECEF. $\boldsymbol{\omega}^e_{ie}$ is the projection of the angular rate of rotation of the Earth in the ECEF-frame. $\boldsymbol{f}^b_{ib}$ is the projection of the force under the b system. $\boldsymbol{\xi}$ is the process noise associated with each state in the state-space model.

Furthermore, Eq. (2) can be written in the following matrix form (xiao et al., 2024):

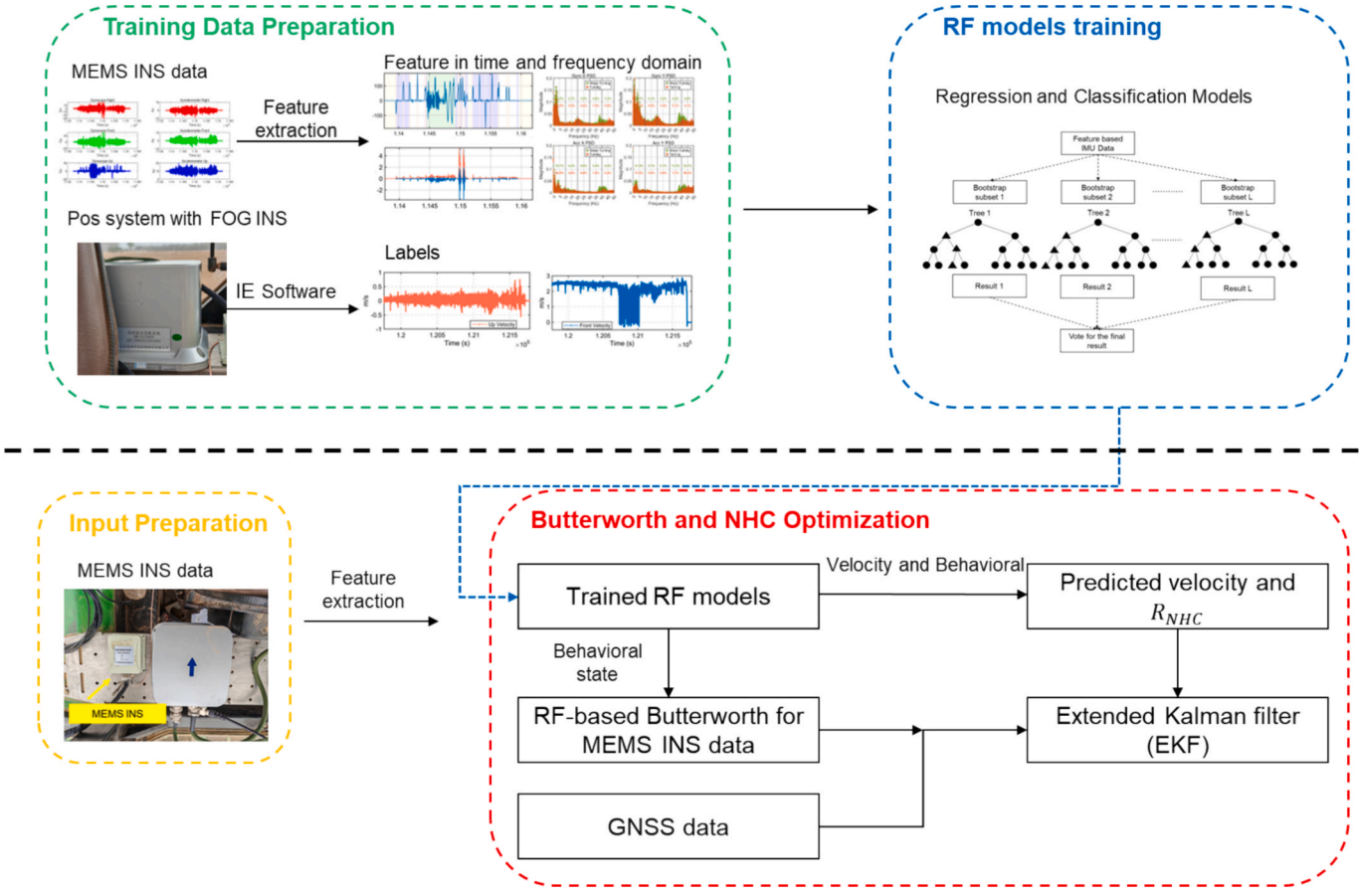

Fig. 1. Framework of the proposed GNSS/MEMS INS TC algorithm.

$$\delta\dot{\boldsymbol{x}}=\begin{bmatrix} -(\boldsymbol{\omega}_{ie}^{e}\times) & \mathbf{0}_{3\times3} & \mathbf{0}_{3\times3} & \mathbf{0}_{3\times3} & -\boldsymbol{C}_{b}^{e} & \mathbf{0}_{3\times n} \\ (\boldsymbol{C}_{b}^{e}\boldsymbol{f}_{ib}^{b})\times & -(2\boldsymbol{\omega}_{ie}^{e}\times) & \mathbf{0}_{3\times3} & \boldsymbol{C}_{b}^{e} & \mathbf{0}_{3\times3} & \mathbf{0}_{3\times n} \\ \mathbf{0}_{3\times3} & \boldsymbol{I}_{3\times3} & \mathbf{0}_{3\times3} & \mathbf{0}_{3\times3} & \mathbf{0}_{3\times3} & \mathbf{0}_{3\times n} \\ \mathbf{0}_{3\times3} & \mathbf{0}_{3\times3} & \mathbf{0}_{3\times3} & \mathbf{0}_{3\times3} & \mathbf{0}_{3\times3} & \mathbf{0}_{3\times n} \\ \mathbf{0}_{3\times3} & \mathbf{0}_{3\times3} & \mathbf{0}_{3\times3} & \mathbf{0}_{3\times3} & \mathbf{0}_{3\times3} & \mathbf{0}_{3\times n} \\ \mathbf{0}_{3\times3} & \mathbf{0}_{3\times3} & \mathbf{0}_{3\times3} & \mathbf{0}_{3\times3} & \mathbf{0}_{3\times3} & \mathbf{0}_{3\times n} \end{bmatrix}\begin{bmatrix} \delta\boldsymbol{\psi}_{eb}^{e} \\ \delta\boldsymbol{v}_{eb}^{e} \\ \delta\boldsymbol{r}_{eb}^{e} \\ \delta\boldsymbol{b}_{a} \\ \delta\boldsymbol{b}_{g} \\ \Delta\nabla\boldsymbol{N}_{rb} \end{bmatrix}+\begin{bmatrix} \boldsymbol{\xi}_{\psi} \\ \boldsymbol{\xi}_{v} \\ \boldsymbol{\xi}_{r} \\ \boldsymbol{\xi}_{ba} \\ \boldsymbol{\xi}_{bg} \\ \boldsymbol{\xi}_{N} \end{bmatrix}=\boldsymbol{F}\delta\boldsymbol{x}+\boldsymbol{w} \tag{3}$$

where $\boldsymbol{F}$ is the state transition matrix. $\delta\boldsymbol{x}$ is the state vector. $\boldsymbol{w}$ is the system noise vector formed by $\boldsymbol{\xi}$, and the widespread successful applications of EKF, UKF and CKF demonstrate that approximating the noise as Gaussian is a reasonable and effective assumption.

2.2.2. Measurement model

The double-difference (DD) observation equation of TC model is given as follows:

$$\begin{cases} \delta\boldsymbol{Z}_{P}=\Delta\nabla\widehat{\boldsymbol{\rho}}-\Delta\nabla\mathbf{P} \\ \delta\boldsymbol{Z}_{\varphi}=\Delta\nabla\widehat{\boldsymbol{\rho}}-\Delta\nabla\varphi+\lambda\Delta\nabla\boldsymbol{N}_{rb} \end{cases} \tag{4}$$

where, $\delta\boldsymbol{Z}_{P}$ and $\delta\boldsymbol{Z}_{\varphi}$ represent the DD residuals of pseudorange and carrier phase, respectively. $\Delta\nabla\mathbf{P}$ and $\Delta\nabla\varphi$ are DD observations of pseudorange and carrier phase, respectively. λ is the wavelength of the carrier observation. $\Delta\nabla\widehat{\boldsymbol{\rho}}$ is the double-difference observations derived from INS, and it involves squared terms and square root operations; therefore, the measurement model is inherently nonlinear.

Since the double-difference (DD) observation equation is nonlinear, and the data fusion algorithm adopted in this paper is the EKF, the double-difference (DD) observation equation must first be linearized, that is, the partial derivatives with respect to the state-space vector are computed to form the Jacobian matrix, which also named design matrix in EKF. After this process, the measurement model, Eq. (4) can be expressed as:

$$\delta\boldsymbol{Z}_{P\ or\ \varphi}=\boldsymbol{H}\delta\boldsymbol{x}+\boldsymbol{R}_{P\ or\ \varphi} \tag{5}$$

where $\boldsymbol{R}_{P\ or\ \varphi}$ represents the measurement noise matrix of the double-difference observations, which can be calculated using the elevation angle model (Bahadur and Schön, 2024. $\delta\boldsymbol{Z}_{P\ or\ \varphi}$ is the measurement vector, and $\boldsymbol{H}$ denotes the design matrix, and the detailed forms are shown in the following equation.

$$\boldsymbol{H}=\begin{bmatrix} \left(\boldsymbol{e}^{k}-\boldsymbol{e}^{1}\right)\left(\boldsymbol{C}_{b}^{e}\boldsymbol{l}^{b}\times\right) & 0 & \boldsymbol{e}^{1}-\boldsymbol{e}^{k} & 0 & 0 & 0 \\ \vdots & \vdots & \vdots & \vdots & \vdots & \vdots \\ \left(\boldsymbol{e}^{k}-\boldsymbol{e}^{n-1}\right)\left(\boldsymbol{C}_{b}^{e}\boldsymbol{l}^{b}\times\right) & 0 & \boldsymbol{e}^{n-1}-\boldsymbol{e}^{k} & 0 & 0 & 0 \\ \left(\boldsymbol{e}^{k}-\boldsymbol{e}^{1}\right)\left(\boldsymbol{C}_{b}^{e}\boldsymbol{l}^{b}\times\right) & 0 & \boldsymbol{e}^{1}-\boldsymbol{e}^{k} & 0 & 0 & \lambda^{1} \\ \vdots & \vdots & \vdots & \vdots & \vdots & \vdots \\ \left(\boldsymbol{e}^{k}-\boldsymbol{e}^{n-1}\right)\left(\boldsymbol{C}_{b}^{e}\boldsymbol{l}^{b}\times\right) & 0 & \boldsymbol{e}^{n-1}-\boldsymbol{e}^{k} & 0 & 0 & \lambda^{n-1} \end{bmatrix} \tag{6}$$

$$\delta\boldsymbol{Z}_{P\ or\ \varphi}=\begin{bmatrix} \Delta\nabla\widehat{\boldsymbol{\rho}}^{1,k}-\Delta\nabla\mathbf{P}^{1,k} \\ \vdots \\ \Delta\nabla\widehat{\boldsymbol{\rho}}^{n-1,k}-\Delta\nabla\mathbf{P}^{n-1,k} \\ \Delta\nabla\widehat{\boldsymbol{\rho}}^{1,k}-\Delta\nabla\varphi^{1,k}+\lambda\Delta\nabla\boldsymbol{N}_{rb}^{1,k} \\ \vdots \\ \Delta\nabla\widehat{\boldsymbol{\rho}}^{n-1,k}-\Delta\nabla\varphi^{n-1,k}+\lambda\Delta\nabla\boldsymbol{N}_{rb}^{n-1,k} \end{bmatrix} \tag{7}$$

where $\boldsymbol{e}^{i}$ denotes the line-of-sight direction vector for satellite i, and $\boldsymbol{l}^{b}$ represents the lever arm. n represents the number of satellites, and $\boldsymbol{\lambda}^{i}$ is a row vector whose dimension corresponds to the number of satellites. Its value is λ for the reference satellite and $-\lambda$ for the other satellites.

2.2.3. The EKF

The procedures of EKF include two steps, as follows:

1) Time update:

$$\delta\widehat{\boldsymbol{x}}_{k,k-1}=\boldsymbol{\phi}_{k,k-1}\delta\widehat{\boldsymbol{x}}_{k-1} \tag{8}$$

$$\boldsymbol{P}_{k,k-1}=\boldsymbol{\phi}_{k,k-1}\boldsymbol{P}_{k-1}\boldsymbol{\phi}_{k,k-1}^{T}+\boldsymbol{Q}_{k-1} \tag{9}$$

where, $\delta\widehat{\boldsymbol{x}}_{k,k-1}$ denotes the predicted state-space vector, and $\boldsymbol{P}_{k,k-1}$ is state error covariance matrix at time k. $\boldsymbol{\phi}_{k,k-1}$ expresses the state transition matrix from time $k-1$ to k. $\delta\widehat{\boldsymbol{x}}_{k-1}$ and $\boldsymbol{P}_{k-1}$ represent the final estimation of the state-space vector and state error covariance matrix at time $k-1$. $\boldsymbol{Q}_{k-1}$ is the system noise matrix at time $k-1$.

2) Measurements update:

$$\delta\widehat{\boldsymbol{x}}_{k}=\delta\widehat{\boldsymbol{x}}_{k,k-1}+\boldsymbol{K}_{k}\left(\boldsymbol{Z}_{k}-\boldsymbol{H}_{k}\delta\widehat{\boldsymbol{x}}_{k,k-1}\right) \tag{10}$$

$$\boldsymbol{P}_{k}=(\boldsymbol{I}-\boldsymbol{K}_{k}\boldsymbol{H}_{k})\boldsymbol{P}_{k,k-1} \tag{11}$$

where $\delta\widehat{\boldsymbol{x}}_{k}$ and $\boldsymbol{P}_{k}$ represent the final estimation of the state-space vector and state error covariance matrix at time k. $\boldsymbol{K}_{k}$ denotes the Kalman gain matrix at time k, which is expressed in Eq. (11). $\boldsymbol{Z}_{k}$ is the measurement vector at time k. $\boldsymbol{H}_{k}$ expresses the design matrix at time k.

$$\boldsymbol{K}_{k}=\boldsymbol{P}_{k,k-1}\boldsymbol{H}_{k}^{T}\left(\boldsymbol{H}_{k}\boldsymbol{P}_{k,k-1}\boldsymbol{H}_{k}^{T}+\boldsymbol{R}_{k}\right)^{-1} \tag{12}$$

where $\boldsymbol{R}_{k}$ is the measurement noise matrix covariance matrix at time k.

2.3. RF for agricultural machinery

The RF in this paper is used for two purposes: (1) classification of agricultural machinery behavioral states and (2) prediction of right and up velocities in the body-frame. Although RF has been widely applied, research on its use in agricultural machinery remains limited. Especially, feature selection for agricultural machinery remains to be investigated. Therefore, this study, for the first time, proposes a set of features for agricultural machinery carriers that are suitable for above two purposes.

2.3.1. Feature configuration

First, the features for behavioral state recognition are introduced, followed by the features for velocity prediction.

(1) Features for behavioral state recognition

According to the operational characteristics of agricultural machinery, behavioral states are divided into six types, as shown in Table 1. The principles for the setting of threshold parameters are described in Gao

Table 1
The threshold parameters for different behavioral states.

State No.	Behavioral State Types	Corresponding practical scenarios	Principles for Threshold Parameters
1	Stop	Initialization, rest	velocity < 0.05 m/s
2	Straight driving	Working	heading rate < 4°/s
3	Braking/ starting	Facing emergency	front acceleration > 0.5 m/ s^2
4	Turning	U-shape turning	heading rate >= 4°/s
5	Sharp turning	S-shape turning, Circular trajectory	heading rate >= 4°/s and turning duration > 15 s
6	Bumping	highly uneven field	vertical velocity > 0.3 m/s

and Zhao (2016) and these parameters are used to compare with the results of the high-precision reference system to generate labels.

The features used for state recognition are categorized by two types: time-domain features and frequency-domain features.

1) Time-domain features

Before introducing the time-domain features, the simple moving-average (*SMA*) will be introduced. This is a commonly used strategy in MEMS INS data processing, aimed at smoothing the raw data, as shown in Eq (13) (Redhyka et al., 2015).

$$data_{SMA,k} = \sum_{k-n+1}^{k} data_{raw,k} \Big/ n \tag{13}$$

where $data_{raw,k}$ represents the INS raw data and $data_{SMA,k}$ is the data which is smoothed by *SMA*. n is the window size, in this paper, n is set as 100.

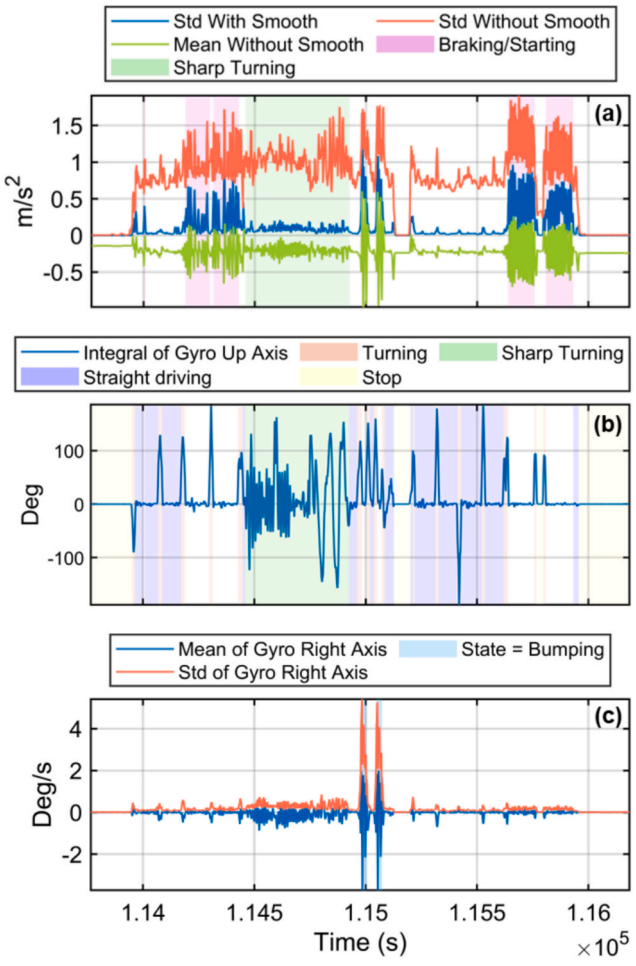

Fig. 2. The time-domain features used for behavioral state recognition.

The purpose of smoothing the data is to promote state identification. For example, as shown in Fig. 2(a), the standard deviation (*Std*) computed from the raw data is represented by the orange line, while the blue line shows the *Std* derived from smoothed data. It can be clearly observed that the orange line shows similar patterns between the braking/starting (purple shadow) and sharp turning (green shadow) states, making it difficult to distinguish the braking/starting state from sharp turning state. In contrast, the blue line exhibits clear characteristics during braking/starting as compared to sharp turning, which allows to easily distinguish between these two states.

Then, the time-domain features used for recognizing each state will be described. First, for the braking/starting states, the most intuitive features are the *Mean* and *Std* of the accelerometer's *y*-axis data, as defined in Eqs. (14) and (15).

$$Mean = \sum_{i-n+1}^{i} data_{raw,i} \Big/ n \tag{14}$$

$$Std = \sqrt{\sum_{i-n+1}^{i} \left(data_{SMA,i} - Mean\right)^2 \Big/ (n-1)} \tag{15}$$

As shown in Fig. 2(a), the *Mean without smooth* (green line) and *Std with smooth* (blue line) of the accelerometer *y*-axis data exhibit significant differences in the braking/starting state (purple shadow). This demonstrates that these features can effectively identify the braking/starting state.

Secondly, the stop, straight driving, turning, and sharp turning, can be effectively distinguished using the integral of the gyroscope *z*-axis, calculated as follows:

$$Integral_{gyro_{up}} = \sum_{i-2n+1}^{i} gyro_{up,raw,i} * dt \tag{16}$$

where dt is the sampling time step, and $gyro_{up,raw,i}$ is the gyroscope raw data about the *z*-axis.

As shown in Fig. 2(b), during the stop, the value of this feature is close to zero; during straight driving, it remains at a low value; during turning, high values appear but last for a short duration; while during sharp turning, the feature maintains a high value and the duration is longer than turning. Therefore, this feature can effectively classify the four behavioral states.

Finally, during bumping state, the gyroscope *x*-axis data shows large value. Therefore, *Mean without smooth* and *Std with smooth* of it are employed, meanwhile, the smoothed data is adopted same as the braking/starting feature extraction. As shown in Fig. 2(c), in blue shadow, the *Mean* and *Std* have a significant difference. This indicates that the feature can effectively identify the bumping state.

2) frequency-domain features

Theoretically, the six behavioral states can be effectively distinguished using above time-domain features. However, in some cases, it still faces challenges. For example, in Fig. 2(b), around 1.15×10^5 s, the integral values show similar characteristics between turning and sharp turning states.

As mentioned in the introduction, in the frequency-domain, different behavioral states exhibit distinct energy distribution patterns of the PSD. Therefore, this study uses energy ratios within 10 Hz intervals from 0 Hz to 50 Hz as new features. Feature extraction requires the use of the Fourier transform, with detailed principles provided in reference (Heideman et al., 1984).

Fig. 3 shows this new feature of turning and sharp turning states. And it shows a significant difference in the band of 30 Hz to 40 Hz, where the percentage of energy distribution during sharp turning significantly exceeds that of turning.

(2) Features for body-frame velocity prediction

The state of agricultural machinery is generally continuous and does

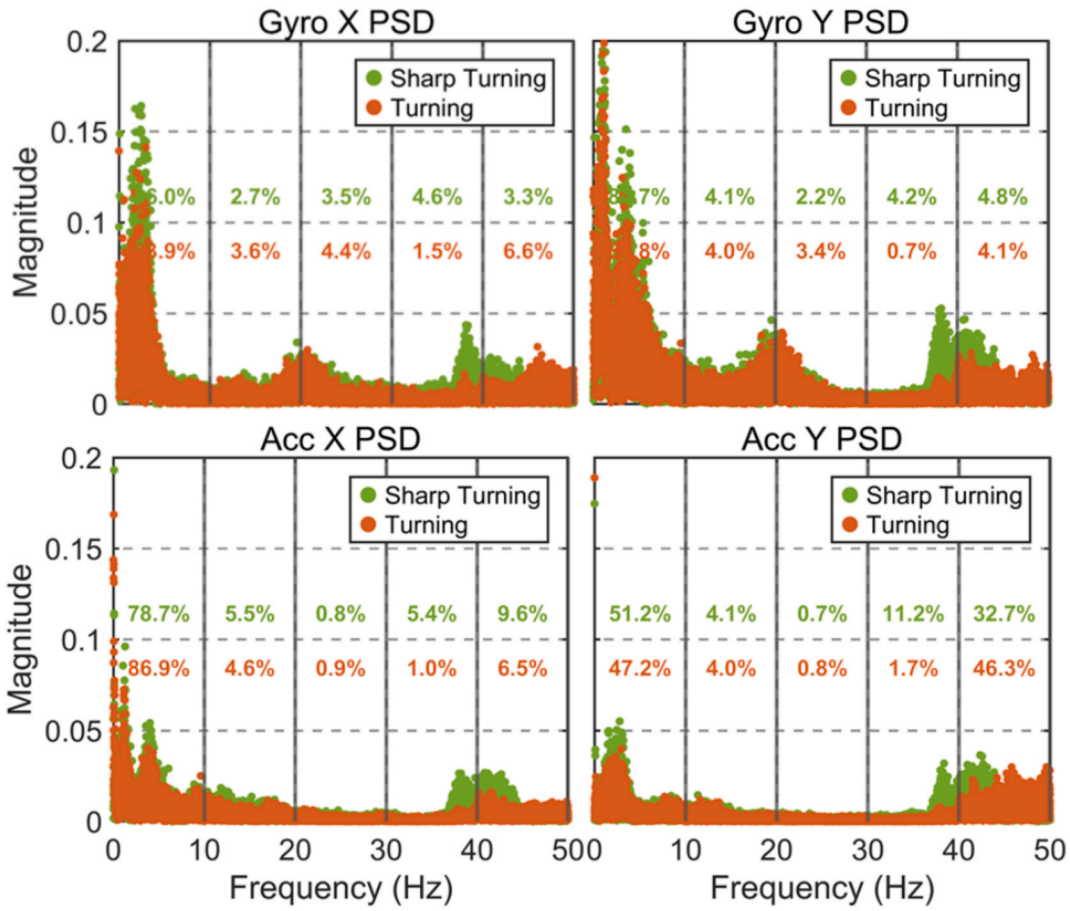

Fig. 3. Energy distribution in frequency domain during sharp turning and turning states.

not change abruptly, whereas the body-frame velocity is affected by uneven terrain and turning, leading to significant variations over a short period. So there are some differences in their feature settings.

For the task of prediction of right and up velocities, this study extracts the *Mean* and *Std* of INS raw data instead of smoothed data, because smoothed data may cause distortion in the predicted speed. The feature extraction methods are described in Eqs. (13) and (14), but the $data_{SMA,i}$ in Eq (14) should be replaced by $data_{raw,i}$.

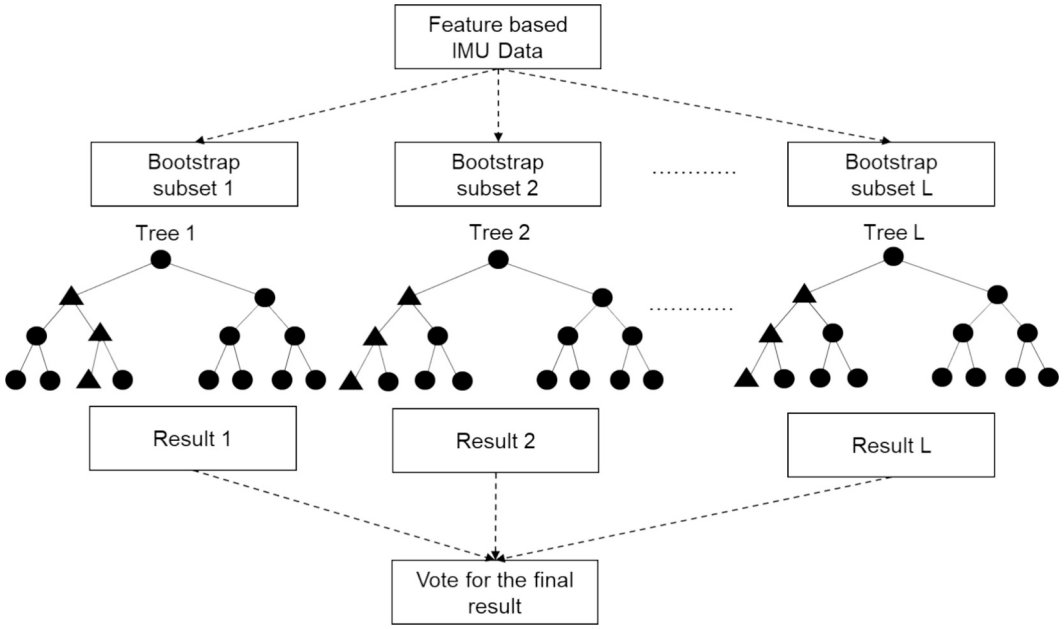

Fig. 4. Flowchart of RF. Circles represent the randomly selected candidate factors and triangles are the optimal splitting factors.

2.3.2. The step of RF

RF is an ensemble learning algorithm which obtains results through voting. In addition, the algorithm exhibits strong randomness in two aspects: 1) The first point lies in the randomness of sampling: n samples are drawn with replacement from the training set to form a subset, and this process is repeated L times to obtain L subsets; 2) The second point lies in the construction of decision trees, where not all features are used; instead, a random subset of the mentioned features is selected for splitting (Breiman, 2001).

The construction processes of RF are shown in Fig. 4, including three main steps:

(1) Step 1: bootstrap resampling. The whole training dataset can be expressed as $\boldsymbol{D} = \{(\boldsymbol{F}_1, y_1), (\boldsymbol{F}_2, y_2), \cdots, (\boldsymbol{F}_N, y_N)\}, N > n$. where $\boldsymbol{F}_i$ represents a feature vector and its dimension is equal to the number of features. y_i is the label used in RF training. In this step, n samples are randomly drawn with replacement from the full dataset to form a training subset, expressed as $\boldsymbol{subset}_i = \{\boldsymbol{D}_1, \boldsymbol{D}_2, \cdots, \boldsymbol{D}_n\}$, $n \in [1, N]$, $i \in [1, L]$.

(2) Step 2: the construction of each decision tree. This step is based on the Classification and Regression Tree (CART) algorithm. For the behavioral state classification task, each decision tree splits in the direction that minimizes the Gini coefficient, which is calculated as follows:

$$Gini = 1 - \left(\sum_{i=1}^{k} p_i^2\right) \tag{17}$$

where p_i is the conditional probability of each behavioral state, and k is the number of states.

For the prediction task of body-frame velocities, CART splits in the direction that minimizes the Mean Squared Error (MSE), which is shown as follows:

$$MSE = \sum_{i=1}^{n} (v_i - \bar{v})^2 \Big/ n \tag{18}$$

where v_i is value of the predicted velocities, $\bar{v}$ is the value of true velocities.

(3) Step 3: the final prediction is obtained through soft voting, with the principle shown in the following equation:

$$Y = \sum_{i=1}^{L} y_i \Big/ L \tag{19}$$

where Y denotes the result of voting.

2.4. RF-based Butterworth filter

This filter was first proposed by Butterworth in 1930, and the principle is shown as follows:

$$|H(\omega)|^2 = 1 \Big/ \left(1 + (\omega/\omega_c)^N\right) \tag{20}$$

where ω is frequency, and ω_c is cutoff frequency. $H(\omega)$ is the amplitude, and N is the order of the filter. Once the cutoff frequency is set, signals with frequencies higher than the cutoff frequency will be filtered out.

As discussed in introduction, among different behavioral states, the PSD of MEMS INS data exhibits different energy distribution characteristics. This causes some states to treat mid-high frequency signals as noise, while in others, the signals in mid-high frequency bands actually reflect the true motion.

To illustrate this point, Fig. 5 shows the PSD of the gyroscope y-axis data under straight driving and bumping states. During the bumping states, the gyroscope y-axis exhibits frequent fluctuations, having a significantly higher energy distribution around 10 Hz compared to the straight driving state. These signals genuinely reflect the roll angle variations during bumping and should not be filtered out. Therefore, the cutoff frequency must be set differently from that of the straight driving state.

To address this limitation, this study proposes, for the first time, a variable-cutoff-frequency Butterworth filter established for typical states in agricultural machinery. Based on the statistical analysis of the PSD of each state, the cutoff frequency settings for each behavioral state are summarized in Table 2. It is worth noting that the following cutoff frequencies are applicable only to agricultural machinery operating in field, and should be treated differently when applied to other scenarios.

Table 2
The cutoff frequency of each behavior context.

	Gyro right	Gyro front	Gyro up	Acc right	Acc front	Acc up
Straight driving	5 Hz	2 Hz	3 Hz	2.5 Hz	5 Hz	5 Hz
Turning	5 Hz	5 Hz	10 Hz	2.5 Hz	5 Hz	5 Hz
Stop	2 Hz	2 Hz	2 Hz	2 Hz	2 Hz	2 Hz
Braking/ starting	5 Hz	2.5 Hz	3.5 Hz	3HZ	5 Hz	5 Hz
Sharp turning	5 Hz	5 Hz	10 Hz	2.5 Hz	5 Hz	5 Hz
Bumping	15 Hz	15 Hz	15 Hz	15 Hz	15 Hz	15 Hz

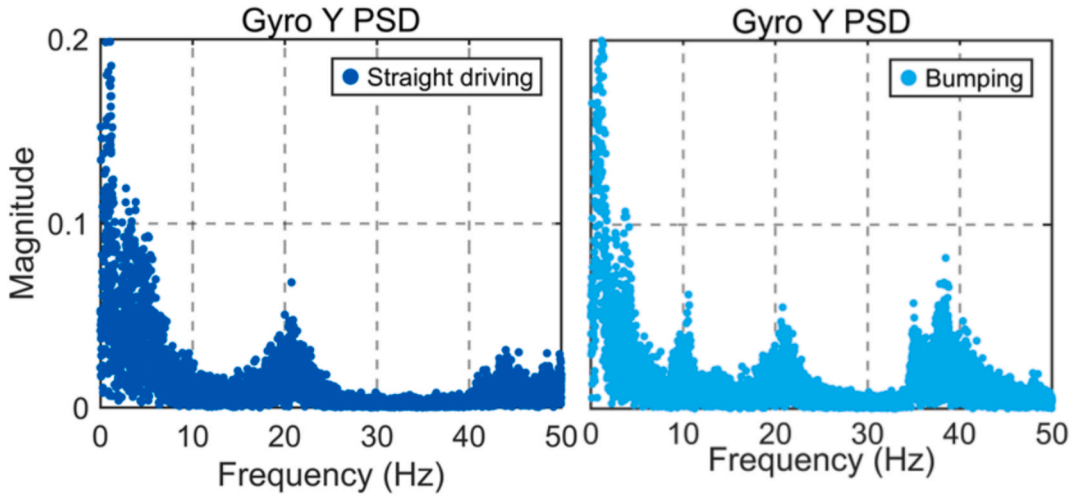

Fig. 5. PSD of the gyroscope y-axis during go straight and bumps states.

2.5. RF-based NHC

In the field of urban vehicle navigation, the NHC assumes that the right and up velocities in the body-frame are approximately zero. However, in agricultural navigation, due to uneven terrain and specific behavioral states, agricultural machinery is more likely to experience jumping and slipping. Especially, the right and up velocities even can exceed 0.5 m/s, and the traditional NHC model cannot be directly applied.

Therefore, this section presents, for the first time, an improved NHC measurement model based on RF-predicted velocity, and a stochastic model refined according to the predicted states. The principles are detailed as follows:

We denote difference between the RF-predicted velocity ($\boldsymbol{v}_{rf}$) and the velocity derived from the MEMS INS ($\boldsymbol{v}_{imu}$) as $\delta\boldsymbol{Z}_{nhc}$, which can be expressed as follows:

$$\delta\boldsymbol{Z}_{nhc} = \boldsymbol{v}_{rf} - \boldsymbol{v}_{imu} = \boldsymbol{H}_{nhc}\delta\boldsymbol{x} + \boldsymbol{R}_{nhc} \tag{21}$$

where $\boldsymbol{H}_{nhc}$ is the design matrix, which is obtained by computing the partial derivative of $\delta\boldsymbol{Z}_{nhc}$ with respect to the state vector (Cheng et al., 2023). $\boldsymbol{R}_{nhc}$ is the measurement noise matrix of the RF-predicted velocity.

Different from $\boldsymbol{R}_{nhc}$ is usually set as constants matrix in traditional NHC algorithms, however, as shown in Figs. 7(b) and (c), the velocity prediction error of the RF (orange lines) is not constant and is strongly correlated with the motion state. Therefore, for the first time, we design a computation equation for $\boldsymbol{R}_{nhc}$, expressed below:

$$\boldsymbol{R}_{nhc} = \begin{cases} \begin{bmatrix} 0.01 & 0 \\ 0 & 0.01 \end{bmatrix} state = 1 \\ \begin{bmatrix} 0.05(state-1)^{\beta} & 0 \\ 0 & 0.03(state-1)^{\beta} \end{bmatrix} state = others \end{cases} \tag{22}$$

where *state* represents the behavioral state, with values from 1 to 6 corresponding to stop, straight driving, braking/starting, turning, sharp turning, and bumping, respectively. The parameter β is set as 0.75 in this study, which, according to test, yields $\boldsymbol{R}$ value that better matches the true errors of the prediction velocities across different behavioral states.

3. Results and discussion

To verify the accuracy of the proposed algorithm, two sets of data were collected, including six behavioral states: stop, straight driving, braking/starting, turning, sharp turning, and bumping. The bumping state was simulated by driving the machinery over bumpy road, as shown in Fig. 6(f). The trajectories of the two datasets are presented in Fig. 6(d) and Fig. 6(e), respectively. The data in Fig. 6(d), lasting 40 min, was used to train the RF model. While the data in Fig. 6(e), lasting 34 min, were used for algorithm evaluation.

The tractor used was the John Deere 904, and the driving speed ranged from 2 to 3 m/s. Two sets of POS devices were installed inside of the cabin, as shown in Fig. 6(a). The high-precision POS called XW-G7680, was used for accuracy evaluation. It includes a fiber optic gyroscope (FOG) INS, with detailed parameters listed in Table 3. Additionally, the high-precision POS is equipped with a UB4B0 GNSS board, which can receive multi-frequency and multi-constellation signals, as shown in Table 4. The reference values for accuracy evaluation were computed by IE Software®.

The other POS, XW-G6615D6, has low-precision POS and was used to evaluate the accuracy of the proposed algorithm. This device consists of the same GNSS board, but a MEMS INS, with parameters listed in Table 3. The base station setup is shown in Fig. 6(b), with an open environment. The rover station antenna setup is illustrated in Fig. 6(c), where the antenna is obstructed by the cabin. This arrangement is intended to verify the robustness of the algorithm by simulating the occluded environment.

Table 3
IMU Parameters in XW-G7680 and XW-G6615D6.

	XW-G6615D6 (MEMS INS)	XW-G7680 (FOG INS)
Bias instability of Gyro (°/h)	10	0.5
Random walk of Gyro (deg/$\sqrt{h}$)	0.7	–
Bias instability of Acc (mg)	0.1	0.1
Random walk of Acc (mg/$\sqrt{Hz}$)	0.5	0.5
Sampling Frequency (Hz)	100	100

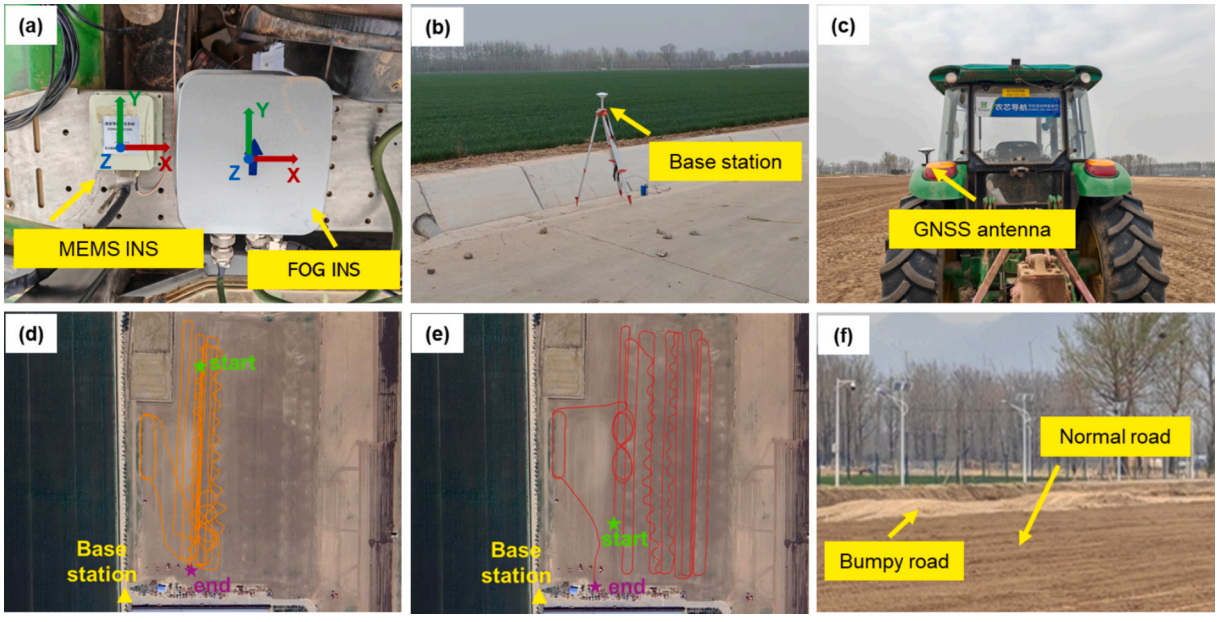

Fig. 6. Overview of the experimental data collection scenarios: (a) pos devices; (b) the environment of base station; (c) the position of GNSS antenna; (d) the trajectory of training data; (e) the trajectory of test data; (f) bumpy road.

Table 4
Parameters of UB4B0.

Signal	BDS B1I/B2I/B3I/B1C/B2a
	GPS L1/L2C/L2P(Y)/L5
	GLONASS G1/G2
	Galileo E1/E5a/E5b
Observation Accuracy	Pseudo-range 10 cm Carrier-phase 1 mm
Positioning Accuracy	SPP 3 m RTK 1.5 cm + 1 ppm

Table 5
The recognition accuracy of each state.

Straight driving	97.93 %
Turning	97.69 %
Stop	98.33 %
Braking/starting	94.50 %
Sharping turning	91.01 %
Bumping	99.79 %

3.1. Performance of RF

The labels used for training the RF model were processed by the IE Software®, which ensures that the training labels are reliable. The basic computer information used for RF model processing are as follows: Intel (R) Core (TM) Ultra 9 CPU@2.30 GHz with 32.0 GB RAM. According to statistics, the average sample testing times for predicting the body-frame right and up velocities are 15.42 ms and 15.88 ms, respectively. The average sample testing time for behavioral state classification is 14.11 ms. Therefore, given the time efficiency, it can meet the real-time requirements of agricultural machinery applications.

Fig. 7(a) illustrates the results of behavioral state recognition, which is based on the low-cost MEMS INS. It can be observed that most of the straight driving states are correctly identified, with only a few misclassified as bumping. However, this does not indicate misclassification. As shown in the bottom-right of Fig. 7(a), some roads during this period were uneven, which may have caused bumping. Then, the turning states are accurately identified, and most sharp turning states are also correctly recognized. However, some misclassifications of sharp turning as normal turning do occur, due to the inherent similarity of features between these two states, which sometimes makes them difficult to distinguish. Next, the recognition results for the braking/starting states are also reasonable. As shown in the top-right corner of Fig. 7(a), these periods exhibit significant fluctuations in front velocity. Then, the bumping state is mainly concentrated on the left side, corresponding to the tractor traversing a bumpy road, as shown in top-left corner of Fig. 7 (a). Finally, the stop state is accurately identified by comparing the stop times. In total, 247,800 behavioral state predictions were obtained, and 238,260 of them were correct, yielding an overall accuracy of 96.15 %. This result includes not only the test data but also 18 % of the validation samples from the training set. As shown in Table 5, the recognition accuracy of each state is also high.

The root mean square errors (RMSE) is given as follows:

$$RMSE = \sqrt{1 \Big/ n \sum_{i=1}^{n} \left(y_i - y_{i,true}\right)^2} \tag{23}$$

where y_i is the calculated value, and $y_{i,true}$ is the true value.

Table 6 shows the RMSE for the predicted right and up velocities, which is classified by state. First, the overall RMSE values are small, indicating that the RF achieves high accuracy in velocity prediction. Second, compared with the calculated values in Eq. (22), the RMSE values in each state are basically consistent, which further verifies the reasonable of the proposed algorithm. Finally, from Figs. 7(b) and (c), the true velocity (orange line) varies with the state. This suggests that assuming the right and up velocities are close to zero, as in the classic NHC model, is unreliable.

To further demonstrate the accuracy of the RF algorithm, it was applied to a second test dataset. This dataset was collected using the XW-G6615D6 mounted on a four-wheeled vehicle, which name is AgileX Hunter2. In addition, the data span is approximately 13 min and was collected in a campus playground environment, which is significantly different from field. The differences between the two datasets can provide stronger evidence for the generalization capability of the RF

Table 6
The RMSE of for the predicted velocities.

	RMSE (m/s)	
	Right	Up
Total	0.05	0.03
Stop	0.01	0.01
Straight driving	0.05	0.02
Braking/starting	0.07	0.04
Turning	0.10	0.07
Sharp turning	0.15	0.08
Bumping	0.17	0.11

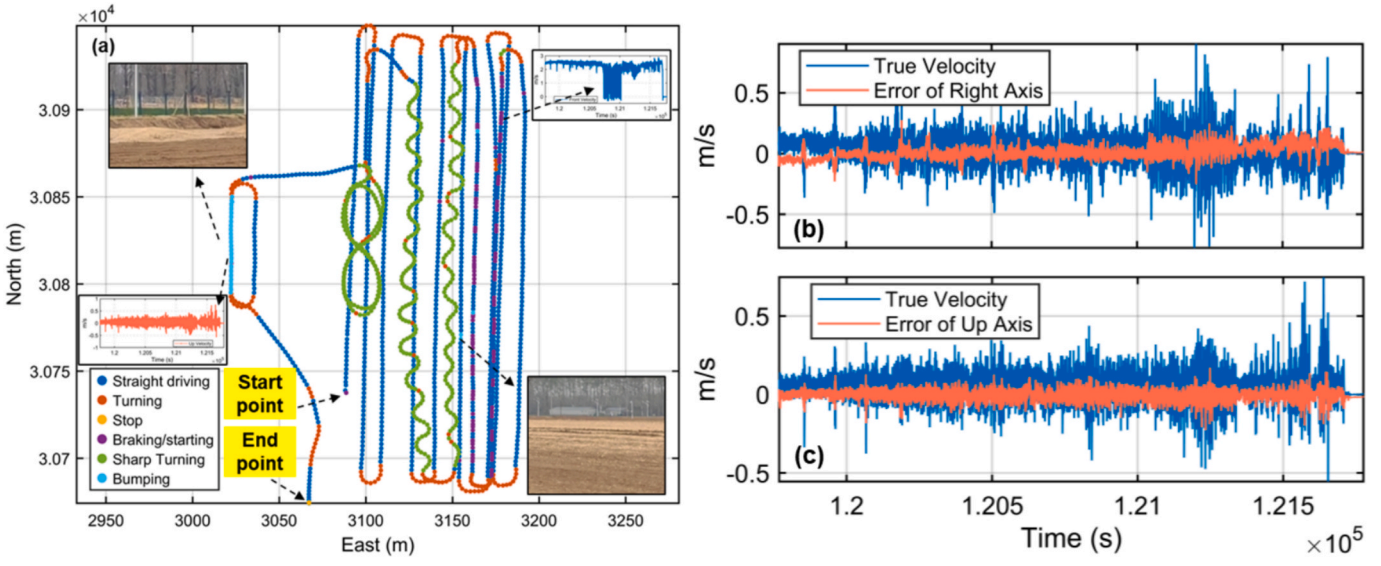

Fig. 7. RF result for behavioral state and body-frame velocities.

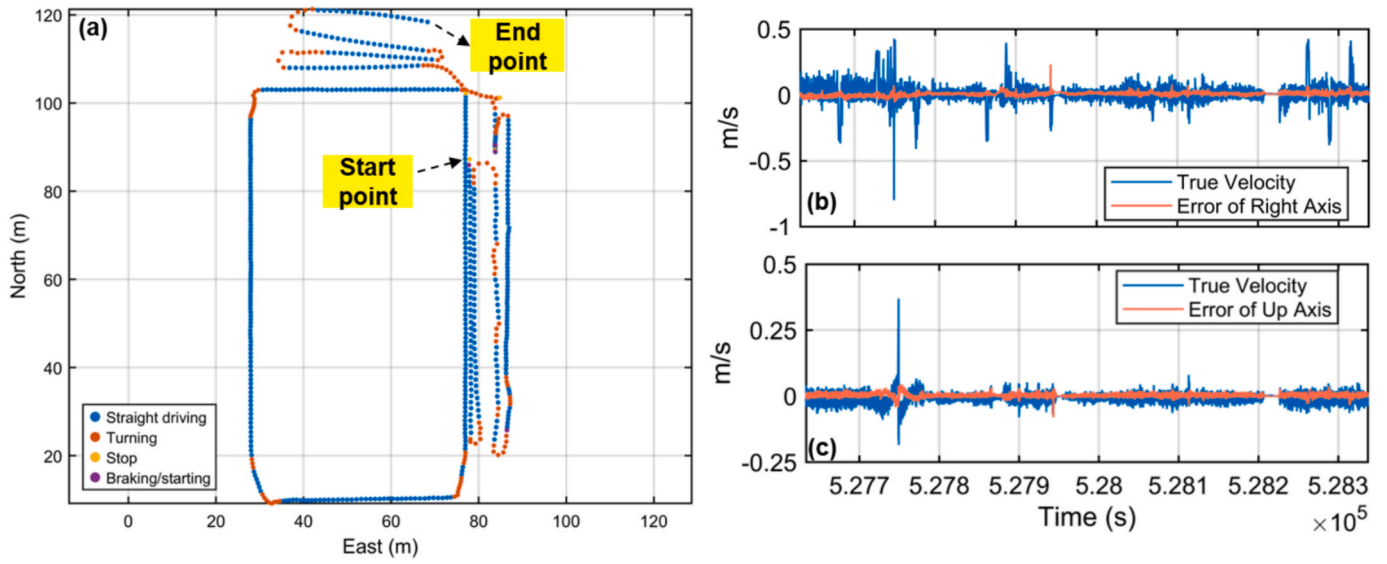

Fig. 8. RF result for behavioral state and body-frame velocities (with additional data).

algorithm.

Since the data were collected in a flat playground environment, only four behavioral states are involved: straight driving, turning, stopping, and braking/starting. As shown in Fig. 8(a), the majority of states were accurately recognized. Compared with the labels computed by the reference system, it was found that even with a different platform and data collection environment, the state recognition accuracy still reached 94.79 %, with a total of 70,400 epochs, of which 66,733 were correctly recognized.

Figs. 8(b) and (c) present the velocity prediction error (orange lines) and the true velocity (blue lines), from which the following conclusions can be drawn: 1) From the blue lines, it can be observed that, compared with Figs. 7(b) and (c), the right and up velocities are significantly smaller because the data were collected in a flatter environment; 2) From the orange lines, it can be seen that the predicted velocity error remains at a low level. Statistical analysis shows that the RMSE of the right velocity is 2 cm/s and that of the up velocity is 1 cm/s.

In summary, using the RF algorithm for both behavioral state recognition and body-frame velocity prediction is feasible, meeting the requirements in terms of both time efficiency and accuracy.

3.2. *Performance of RF-based Butterworth filter*

This section evaluates the accuracy of three schemes: 1) TC algorithm using raw MEMS INS data; 2) TC algorithm using MEMS INS data, which is filtered by classic Butterworth filter; 3) TC algorithm, which is filtered by RF-based Butterworth filter. Note that the accuracy assessment is based on the NEU coordinate system, with the reference station as the origin. Here, N represents the north direction, E the east direction, and U the up direction.

From Fig. 9, the findings can be listed as follows:

1) The state before 1.21x10^{5}s mainly corresponds to straight driving state. Under this condition, Schemes 2 and 3 exhibit similar accuracy, both of them show better accuracy than Scheme 1. This is because straight driving state is the main state in the overall data. Therefore, the uniform cutoff frequency of classic Butterworth filter is close to the cutoff frequency of RF-based filter during straight

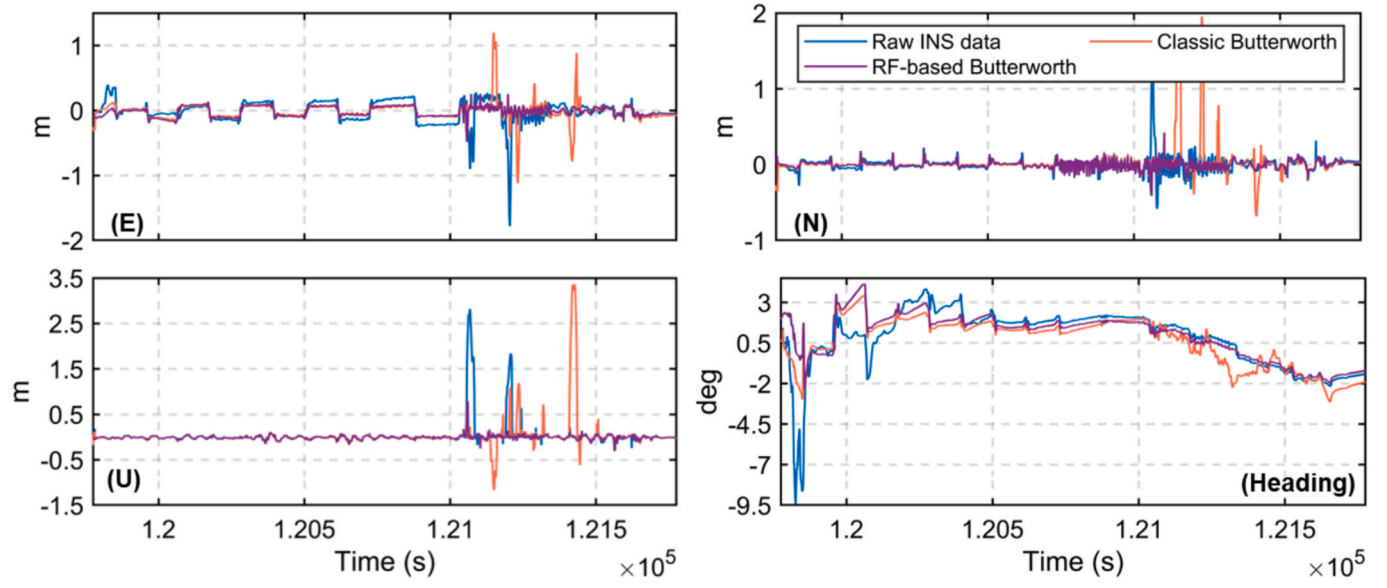

Fig. 9. Positioning and heading errors, for comparison with the RF-based Butterworth filter.

driving. Therefore, both algorithms have similar accuracy in this state.

2) Between $1.21x10^5$s and $1.215x10^5$s, the navigation accuracy of Scheme 1 decreases. There are two main reasons: Firstly, As is well known, the accuracy of MEMS INS mechanization is highly correlated with the motion state of the vehicle, and it degrades significantly under sharp turning conditions; Then, the rover antenna was installed on the side of the cabin, as shown in Fig. 6(c). This arrangement caused frequent changes in the number of common-view satellites between the rover antenna and the base antenna during sharp turns. These two factors together led to the accuracy degradation of scheme 1.
3) Between $1.21x10^5$s and $1.215x10^5$s, a significant increase in positioning errors was observed for Scheme 2, with positioning errors in the N and U directions even exceeding those of Scheme 1. As discussed in Section 2.4, during this period tractor is in sharp turning and bumping states. When using the classic Butterworth filter, some mid-frequency signals, such as those around 10 Hz shown in Fig. 5, are filtered out. These signals objectively reflect the current variations in tractor velocity and angular velocity. By removing these critical mid-frequency signals, Scheme 2 causes distortion in the positioning accuracy.
4) Between $1.21x10^5$s and $1.215x10^5$s, Scheme 3 employs RF-based Butterworth filter. During sharp turning and bumping states, it effectively preserves mid-frequency signals that reflect the true motion. As a result, it makes Scheme 3 have the best accuracy, demonstrating the superiority of the RF-based Butterworth filter.
5) Finally, analysis of the heading error leads to a similar conclusion: the classic Butterworth filter method improves accuracy during straight driving states but performs poorly during sharp turning and bumping states. The optimized algorithm achieves the best accuracy across all behavioral states.

Table 7 presents the RMSE of the positioning in the ENU direction and heading errors. The results show the following: 1) Scheme 2, compared with Scheme 1, does not improve positioning accuracy, and achieves a 20.3 % improvement in heading accuracy. 2) Scheme 3 significantly outperforms Scheme 1, with positioning accuracy improved by 52.9 %, 54.5 %, and 83.3 % in the East, North, and Up directions, respectively. Additionally, heading accuracy is improved by 23.3 %.

3.3. Performance of RF-based NHC

In this section, the MEMS INS data were processed using the RF-based Butterworth filter. Four Schemes were employed in this section: 1) without NHC; 2) using the classic NHC (right and up velocities are setting as zero); 3) using the RF-predicted velocities (without adjusting the $\boldsymbol{R}_{nhc}$); 4) RF-based NHC (the behavioral states are used to adjust the $\boldsymbol{R}_{nhc}$).

Fig. 10 presents the errors of positioning, velocity, and heading for the four schemes, and the findings can be listed as follows:

1) Before $1.21x10^5$s, the main states of the tractor are straight driving. During this period, the positioning accuracy of all schemes, in descending order, is: Scheme 4, Scheme 3, Scheme 2, Scheme 1. There are some reasons for this order. At first, during the straight driving, the true right and up body-frame velocities are closer to zero than other states, making the zero-velocity assumption somewhat reasonable, which improves its positioning accuracy over Scheme 1. Secondly, Scheme 3 uses RF-predicted velocities, which provide a more accurate velocities than Scheme 2, thus yielding better accuracy. Scheme 4 achieves the best accuracy due to the combination of both the optimized measurement model and the adaptive stochastic model.
2) Before $1.21x10^5$s, velocity accuracy of Scheme 2 degrades mainly during turning, where large right velocity violates the zero-velocity assumption of the classic NHC. This causes incorrect corrections and reduces accuracy. As shown in Fig. 10, the velocity errors with classic NHC are clearly larger than those without NHC, especially during turning states.
3) Between $1.21x10^5$s and $1.215x10^5$s, corresponding to the sharp turning and bumping states. Unlike in the straight driving case, Scheme 2 performs worse than Scheme I. Reasons are as follows: as shown in Figs. 7(b) and 7(c), the average body-frame velocities reach approximately 0.5 m/s. Therefore, the measurement model of Scheme 2, which assumes velocities are close to zero, becomes entirely invalid, resulting in a significant decrease in accuracy.
4) From the velocity and heading error sequences, similar conclusions can be drawn: Schemes 2 and 3 exhibit better accuracy than Scheme 1 before $1.21x10^5$s. During sharp turning and bumping states, Schemes 2 and 3 suffer from inaccurate measurement or stochastic models, resulting in reduced accuracy, unfortunately sometimes even worse than Scheme 1. In contrast, Scheme 4, benefiting from accurate measurement and stochastic models, maintains the best accuracy throughout the entire period.

Table 7
RMSE of positioning and Heading errors. Note that percentage improvement is relative to Raw INS data.

	East (cm)	North (cm)	Up (cm)	3D (cm)	Heading (deg)
Raw INS data	17	11	30	36	2.02
Classic Butterworth	14(17.6 %)	19	33	40	1.61(20.3 %)
RF-based Butterworth	8(52.9 %)	5(54.5 %)	5(83.3 %)	11(69.4 %)	1.55(23.3 %)

As shown in Table 8, the following conclusions can be drawn: 1) Compared to Scheme 1, Scheme 2 achieves 32.9 % improvement in heading accuracy. However, the positioning and velocity accuracy significantly degrades. This is because the incorrect velocity affects the accuracy; 2) Scheme 3 outperforms Schemes 1 and 2. However, due to the limited accuracy of the stochastic model during sharp turning and bumping states, compared to Scheme 1, the improvement in velocity is limited; 3) Scheme 4 shows significant improvements in positioning, velocity, and heading estimation compared to Scheme 1, with increases of 36.4 %, 22.3 %, and 78.7 %, respectively. These improvements are attributed to the comprehensive optimization of both the measurement and stochastic models.

To further demonstrate the performance of the RF-based NHC algorithm, this section adds a comparative experiment within the time interval from $1.21x10^5$s to the end, using the following algorithms: 1) TC algorithm; 2) Classic NHC algorithm with the R matrix parameter set to 0.1; 3) Classic NHC algorithm with the R matrix parameter set to 0.5; 4) Classic NHC algorithm with the R matrix parameter set to 1; 5) RF-based NHC.

Fig. 11 presents the errors of positioning and heading for the five schemes, and the findings can be listed as follows:

1) Since this period corresponds to sharp turning and bumping of agricultural machinery, the velocities in the right and up directions are excessively large. Therefore, when the parameter of the R matrix was set to 0.1, the inaccurate observation model was overly trusted. As a result, the case with R = 0.1 (orange lines) exhibited many spikes, and its errors were even larger than those of the TC algorithm (blue lines) without NHC.
2) For R = 0.5 (purple lines) and R = 1 (green lines). As shown in the black enlarged view indicated by the black arrow, it can be clearly observed that at the time points when the TC algorithm (blue lines) exhibits large errors, the accuracy of these two methods is also poor, and the three methods show comparable accuracy. This is because

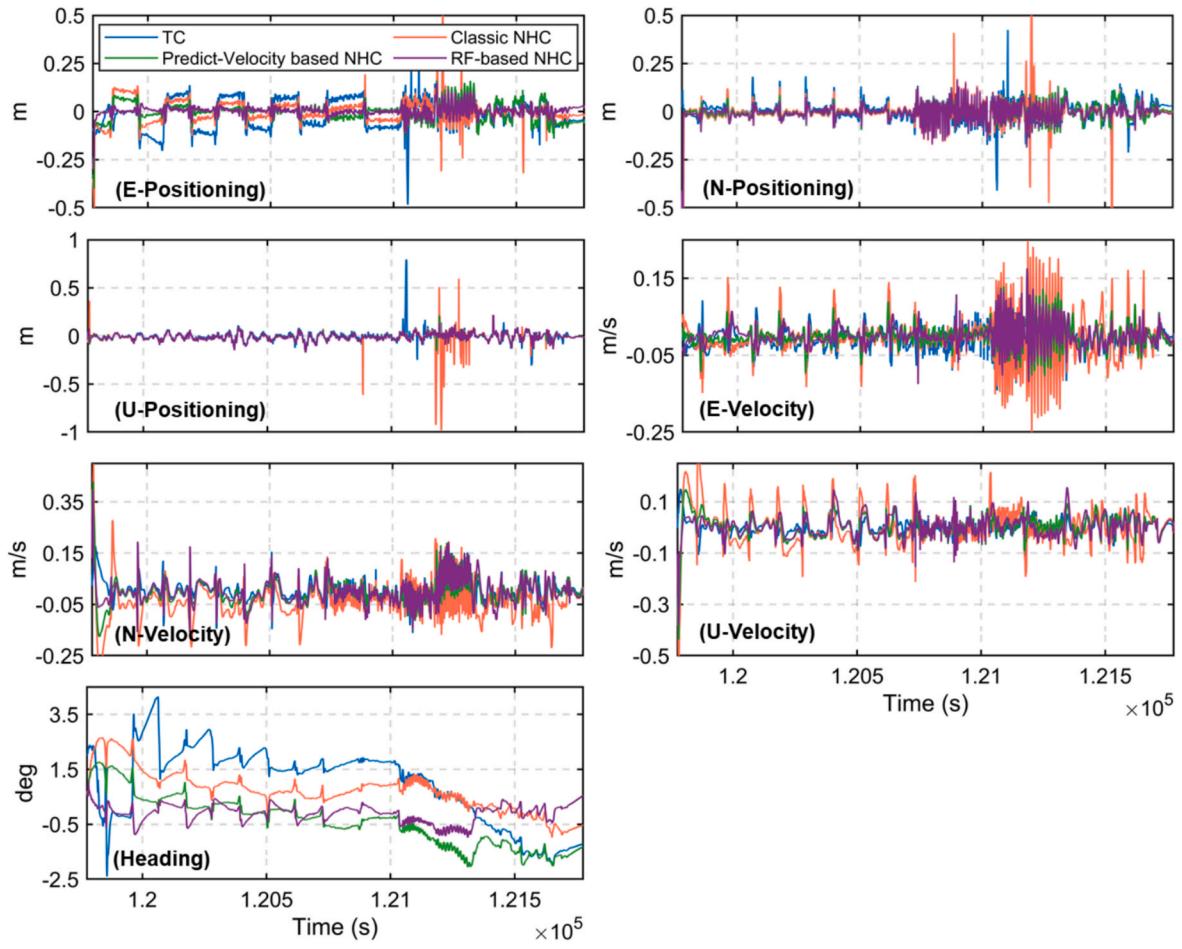

Fig. 10. Positioning, velocity and heading errors, for comparison with the RF-based NHC.

Table 8
RMSE of positioning, velocity and heading errors. Note that percentage improvement is relative to TC.

	East (cm)	North (cm)	Up (cm)	East (cm/s)	North (cm/s)	Up (cm/s)	Heading (deg)
TC	8	5	5	4	4	4	1.55
Classic NHC	6 (25 %)	7	8	5	8	8	1.04 (33 %)
Predict-Velocity NHC	5 (38 %)	5	4 (20 %)	3 (25 %)	5	5	0.99 (36 %)
RF-based NHC	3 (63 %)	5	4 (20 %)	2 (25 %)	3 (25 %)	4	0.33 (79 %)

when R is set to 0.5 and 1, the fusion algorithm no longer over-trusts the classic NHC observation model. Therefore, the accuracy becomes close to that of the TC algorithm.

3) The algorithm proposed in this paper (yellow lines) achieves the best performance in both positioning accuracy and heading accuracy, which demonstrates the correctness of its mathematical model.

From Table 9, the following conclusions can be drawn: 1) When R = 0.1, the positioning accuracy decreases, for the same reasons as analyzed in Fig. 10. Interestingly, however, the heading accuracy improves. 2) When R = 0.5, both positioning and heading accuracies show moderate improvement, indicating that the classic NHC can achieve a slight accuracy gain by increasing the R parameter. 3) When R = 1, since the fusion algorithm no longer trusts the NHC model, the accuracy remains almost unchanged. 4) The algorithm proposed in this paper achieves a significant improvement in both positioning and heading accuracy compared with the TC algorithm, which benefits from obtaining the most accurate mathematical model through RF-based prediction.

4. Conclusion

This study proposes a GNSS/MEMS INS tightly coupled navigation algorithm for agricultural environments with severe occlusions. To address the limitations of traditional Butterworth filter and NHC when applied to uneven farmland and the unique maneuvers of agricultural machinery, we introduce several targeted improvements.

First, we identify that accurate behavioral-state and body-frame velocity perception is essential for enhancing both algorithms. An RF-based behavioral awareness model is therefore developed, with distinct feature sets designed for state recognition and velocity prediction. Second, the Butterworth filter is adapted by assigning different cutoff frequencies according to RF-predicted states, mitigating the signal distortion commonly observed in traditional Butterworth filter. Finally, RF-predicted velocities are used to replace the inaccurate observation equation in traditional NHC, while its stochastic model is adaptively adjusted based on the recognized state. Using the proposed method, the agricultural vehicle attains centimeter-level positioning accuracy and a heading accuracy of 0.33°, which is sufficient for practical agricultural navigation tasks.

The accuracy of behavioral-state recognition and velocity prediction in the RF model is crucial to the performance of the proposed method.

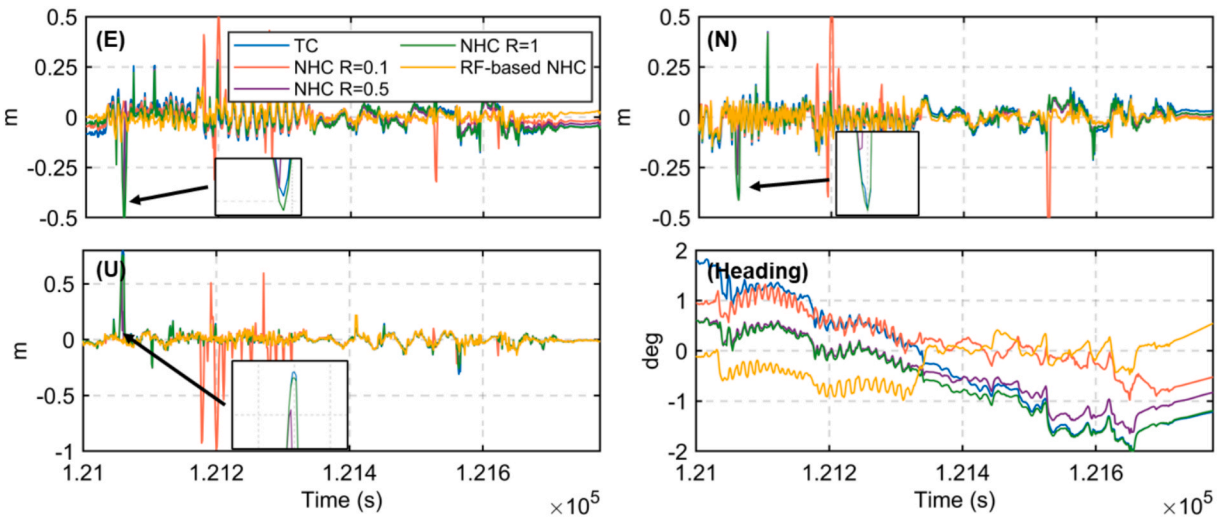

Fig. 11. Positioning and heading errors, for comparison with the Classic NHC algorithm with different R matrix.

Table 9
RMSE of positioning and heading errors. Note that percentage improvement is relative to TC.

	East (cm)	North (cm)	Up (cm)	3D (cm)	Heading (deg)
TC	7	6	8	12	1.14
NHC R = 0.1	6 (14.3 %)	8	11	15	0.61 (46.5 %)
NHC R = 0.5	5 (28.6 %)	5 (16.7 %)	7(12.5 %)	10 (16.7 %)	0.78 (31.6 %)
NHC R = 1	7	6	7 (12.5 %)	12	1.01 (11.4 %)
RF-based NHC	3 (57.2 %)	3 (50 %)	4 (50 %)	6 (50 %)	0.41 (64.1 %)

Although the RF model achieves high accuracy on the two available test sets, its generalization ability still requires further validation due to the limited amount of training data. Future work will focus on collecting more diverse datasets to improve the robustness and generality of the RF model. In addition, although the proposed method outperforms traditional algorithms during sharp turning and bumping, its accuracy in highly dynamic scenarios is still limited by the linearization errors of the EKF framework. Future research will explore the use of UKF or CKF to address performance degradation under high-dynamic agricultural operations.

CRediT authorship contribution statement

Yihang Feng: Writing – original draft, Validation, Methodology. **Guanwen Huang:** Writing – review & editing, Funding acquisition. **Mingfeng Wang:** Writing – review & editing, Supervision, Methodology. **Xin Li:** Writing – review & editing, Methodology. **Zhenhong Li:** Funding acquisition. **Hang Li:** Methodology, Data curation. **Kai Zhang:** Data curation. **Ce Jing:** Writing – review & editing.

Declaration of competing interest

The authors declare that they have no known competing financial interests or personal relationships that could have appeared to influence the work reported in this paper.

Acknowledgements

This work was supported by the Programs of the National Natural Science Foundation of China (42374025). This work was also supported by the Program of China Scholarship Council (CSC) under Grant 202406560066.

Data availability

Data will be made available on request.

References

Bahadur, B., Schön, S., 2024. Improving the stochastic model for code pseudorange observations from Android smartphones. GPS Solut. 28, 148.
Breiman, L., 2001. Random forests. Mach. Learn. 45 (1), 5–32.
Cheng, S., Cheng, J., Zang, N., et al., 2023. Adaptive non-holonomic constraint aiding multi-GNSS PPP/INS tightly coupled navigation in the urban environment. GPS Solut. 27, 152.
Cui, B., Wang, J., Li, P., Hu, J., Zuo, X., Tang, L., 2025. Modified ionosphere delay fitting model with atmosphere uncertainty grids for wide-area real-time positioning. Geo-spatial Inf. Sci. 1–19.
Feng, Y., Huang, G., Jing, C., et al., 2023. GNSS/MEMS IMU vehicle integrated navigation algorithm constrained by displacement vectors in urban environment. Meas. Sci. Technol. 34 (12), 125157.
Feng, Y.H., Huang, G.W., et al., 2025. Dual-Antenna GNSS/MEMS INS tightly coupled algorithm for agricultural machinery based on adaptive federated filtering. IEEE Sens. J. 25 (9), 14780–14792.
Gao, S., Zhong, Y., Hu, G., Gao, B., 2015. Windowing and random weighting-based adaptive unscented Kalman filter. Int. J. Adapt Control Signal Process. 29 (2), 201–223. https://doi.org/10.1002/acs.2467.
Gao, N., Zhao, L., 2016. An integrated land vehicle navigation system based on context awareness. GPS Solut. 20, 509–524.
Gao, B., Gao, S., Zhong, Y., et al., 2017. Interacting multiple model estimation-based adaptive robust unscented Kalman filter. Int. J. Control Autom. Syst. 15, 2013–2025.
Guo, J., Li, X., Li, Z.H., et al., 2018. Multi-GNSS precise point positioning for precision agriculture. Precis. Agric. 19, 895–911.
Gao, Z., Gu, C., Yang, J., Gao, S., Zhong, Y., 2020. Random weighting-based nonlinear Gaussian filtering. IEEE Access 8, 19590–19605.
Gao, B., Hu, G., Zhong, Y., Zhu, X., 2021a. Cubature rule-based distributed optimal fusion with identification and prediction of kinematic model error for integrated UAV navigation. Aerosp. Sci. Technol. 109, 106447.
Gao, B., Hu, G., Zhong, Y., Zhu, X., 2021b. Cubature Kalman filter with both adaptability and robustness for tightly-coupled GNSS/INS integration. IEEE Sens. J. 21 (13), 14997–15011.
Gao, B., Li, W., Hu, G., Zhong, Y., Zhu, X., 2022. Mahalanobis distance-based fading cubature Kalman filter with augmented mechanism for hypersonic vehicle INS/CNS autonomous integration. Chin. J. Aeronaut. 35 (5), 114–128.
Gao, G., Gao, S., Hu, G., et al., 2023a. Tightly coupled INS/CNS/spectral redshift integrated navigation system with the aid of redshift error measurement. Sci. China Technol. Sci. 66, 2597–2610.
Gao, B., Hu, G., Zhang, L., Zhong, Y., Zhu, X., 2023b. Cubature Kalman filter with closed-loop covariance feedback control for integrated INS/GNSS navigation. Chin. J. Aeronaut. 36 (5), 363–376.
Heideman, M., Johnson, D., Burrus, C., 1984. Gauss and the history of the fast Fourier transform. IEEE ASSP Mag. 1, 14–21.
Hu, G., Gao, S., Zhong, Y., 2015a. A derivative UKF for tightly coupled INS/GPS integrated navigation. ISA Trans. 56, 135–144.

Hu, G., Gao, S., Zhong, Y., Gao, B., 2015b. Stochastic stability of the derivative unscented Kalman filter. Chin. Phys. B 24 (7), 070202.
Hu, G., Gao, S., Zhong, Y., Gao, B., 2015c. Modified strong tracking unscented Kalman filter for nonlinear state estimation with process model uncertainty. Int. J. Adapt Control Signal Process. 29 (12), 1561–1577.
Hu, G., Wang, W., Zhong, Y., Gao, B., Gu, C., 2018. A new direct filtering approach to INS/GNSS integration. Aerosp. Sci. Technol. 77, 755–764.
Hu, G., Gao, B., Zhong, Y., Ni, L., Gu, C., 2019. Robust unscented Kalman filtering with measurement error detection for tightly coupled INS/GNSS integration in hypersonic vehicle navigation. IEEE Access 7, 151409–151421.
Hu, Z.K., Zhu, F., Liu, W.K., 2020a. Dual antenna GNSS/MEMS integration attitude determination with Butterworth filter smoothed accelerometer. J. Geod. Geodyn. 40 (1), 51–55 in Chinese.
Hu, G., Gao, B., Zhong, Y., Gu, C., 2020b. Unscented Kalman filter with process noise covariance estimation for vehicular INS/GPS integration system. Inf. Fusion 64, 194–204.
Hu, G., Ni, L., Gao, B., Zhu, X., Wang, W., Zhong, Y., 2020c. Model predictive based unscented Kalman filter for hypersonic vehicle navigation with INS/GNSS integration. IEEE Access 8, 4814–4823.
Huang, Y., Fu, J., Xu, S., Han, T., Liu, Y., 2022. Research on integrated navigation system of agricultural machinery based on RTK-BDS/INS. Agriculture 12 (8), 1169.
Huang, G.W., Du, S., Wang, D., 2023. GNSS techniques for real-time monitoring of landslides: A review. Satell. Navig. 4 (5).
Hu, G., Xu, L., Gao, B., Chang, L., Zhong, Y., 2023. Robust unscented Kalman filter-based decentralized multisensor information fusion for INS/GNSS/CNS integration in hypersonic vehicle navigation. IEEE Trans. Instrum. Meas. 72, 1–11.
Hu, G., Xu, L., Yang, Z., Gao, B., Zhong, Y., 2024. Indirect fuzzy robust cubature-Kalman filter with normalized input parameters. IEEE Trans. Aerosp. Electron. Syst. 60 (5), 5880–5890.
Hu, G., Geng, J., Chang, L., Gao, B., Zhong, Y., 2025. Tightly coupled SINS/DVL based on lie group SE2(3) in local-level frame. IEEE Trans. Aerosp. Electron. Syst.
Jiang, A.L., Ahamed, T., 2025. Development of an autonomous navigation system for orchard spraying robots integrating a thermal camera and LiDAR using a deep learning algorithm under low- and no-light conditions. Comput. Electron. Agric. 235, 110359.
Jing, C., Bertolesi, E., Huang, G.W., et al., 2025. Predicting accelerometer baseline correction and nondivergent deformation velocity based on convolutional neural network (CNN) during GNSS downgrade. IEEE Sens. J. 25 (7), 11982–11994.
Kirsch, K., Strutzke, S., Klitzing, L., Pilger, F., Thöne-Reineke, C., Hoffmann, G., 2025. Validation of a time-distributed residual LSTM–CNN and BiLSTM for equine behavior recognition using collar-worn sensors. Comput. Electron. Agric. 231, 109999.
Lai, W., Huang, G.W., Wang, L., et al., 2025. Real-time high-precision joint orbit determination of GPS and LEO using SRIF. Meas. Sci. Technol. 36, 5.
Li, S.C., Zhang, M., Ji, Y.H., Zhang, Z.Q., Cao, R.Y., Chen, B., Li, H., Yin, Y.X., 2021a. Agricultural machinery GNSS/IMU-integrated navigation based on fuzzy adaptive finite impulse response Kalman filtering algorithm. Comput. Electron. Agric. 191, 106524.
Li, S., Zhang, M., Cao, R., Ji, Y., Zhang, Z., Li, H., Yin, Y., 2021b. Development of the automatic navigation system for combine harvester based on GNSS. Int. J. Agric. Biol. Eng. 14 (5), 163–171.
Li, X., Wang, X., Liao, J., et al., 2021c. Semi-tightly coupled integration of multi-GNSS PPP and S-VINS for precise positioning in GNSS-challenged environments. Satell. Navig. 2, 1.
Li, X., Li, H.X., Huang, G.W., et al., 2023. Non-holonomic constraint (NHC)-assisted GNSS/SINS positioning using a vehicle motion state classification (VMSC)-based convolution neural network. GPS Solut. 27, 144.
Li, L., Xu, Z., Jia, Z., et al., 2024. An efficient GNSS NLOS signal identification and processing method using random forest and factor analysis with visual labels. GPS Solut. 28, 77.
Lü, E., Wei, J., Wang, Y., Zhao, J., Wang, F., Liu, Y., 2018. Trajectory tracking algorithm of autonomous mobile platform for animal husbandry environment information monitoring. Trans. Chin. Soc. Agric. Eng. 34 (13), 86–94.
Lü, E., Su, Q., Wang, F., Luo, Y., Zeng, B., Zeng, Z., 2022. Mapping and localization of animal husbandry autonomous mobile robot based on Apriltag. J. Chin. Agric. Mech. 43 (4), 138–145 in Chinese.
Niu, X., Nassar, S., Na, E.S., 2007. An accurate land-vehicle MEMS IMU/GPS navigation system using 3D auxiliary velocity updates. Navigation 54 (3), 177–188.
Niu, X.J., Ban, Y.L., Zhang, T.S., Liu, J.N., 2016. Research progress and prospects of GNSS/INS deep integration. Acta Aeronaut. Astronaut. Sin. 37 (10), 2895–2908 in Chinese.
Peng, Y.Q., Kondo, N., Fujiura, T., Suzuki, T., Ouma, S., Wulandari, et al., 2020. Dam behavior patterns in Japanese black beef cattle prior to calving: Automated detection using LSTM-RNN. Comput. Electron. Agric. 169, 105178.
Rahman, A., Smith, D.V., Little, B., Ingham, A.B., Greenwood, P.L., Bishop-Hurley, G.J., 2018. Cattle behaviour classification from collar, halter, and ear tag sensors. Inf. Process. Agric. 5 (1), 124–133.
Rafatnia, S., Nourmohammadi, H., Keighobadi, J., 2019. Fuzzy-adaptive constrained data fusion algorithm for indirect centralized integrated SINS/GNSS navigation system. GPS Solut. 23 (3).
Redhyka, G.G., Setiawan, D., Soetraprawata, D., 2015. Embedded sensor fusion and moving-average filter for Inertial Measurement Unit (IMU) on the microcontroller-based stabilized platform. Proc. ICACOMIT. 72–77.
Rohac, J., Reinstein, M., Draxler, K., 2011. Data processing of inertial sensors in strong-vibration environment. Proc. 6th IEEE Int. Conf. Intell. Data Acquis. Adv. Comput. Syst., Prague, Czech Republic, 71–75.
Sun, R., Yang, Y., Chiang, K.W., Duong, T.T., Lin, K.Y., Tsai, G.J., 2020. Robust IMU/GPS/VO integration for vehicle navigation in GNSS degraded urban areas. IEEE Sens. J. 20 (17), 10110–10122.
Sun, Y., Li, Z., Yang, Z., et al., 2022. Motion model-assisted GNSS/MEMS-IMU integrated navigation system for land vehicle. GPS Solut. 26, 131.
Wang, L., Niu, X., Zhang, T., Tang, H., Chen, Q., 2022. Accuracy and robustness of ODO/NHC measurement models for wheeled robot positioning. Measurement 201, 111720–111729.
Wang, D., Huang, G.W., Du, Y., et al., 2023. Stability analysis of reference station and compensation for monitoring stations in GNSS landslide monitoring. Satell. Navig. 4, 29.
Wu, F., Yang, Y., 2007. GPS/INS integrated navigation by adaptive filtering based on wavelet threshold de-noising. Acta Geodaetica et Cartographica Sinica. 2007 (02), 10–14 in Chinese.
Xu, A.G., Liu, T., Sui, X., Hao, Y.S., Yang, D.H., Guo, Z., Wang, C.Q., 2018. A method of GPS/INS tightly coupled in low dynamic and high jitter environment. Sci. Surveying Mapping. 43 (2), 1–5 in Chinese.
Xie, B.B., Jin, Y.C., Faheem, M., Gao, W.J., Liu, J.Z., Jiang, H.K., Cai, L.J., Li, Y.X., 2023. Research progress of autonomous navigation technology for multi-agricultural scenes. Comput. Electron. Agric. 211, 107963.
Xiao, K., Sun, F., Zhu, X., et al., 2024. Assessment of overlapping triple-frequency BDS-3/BDS-2/INS tightly coupled integration model in kinematic surveying. GPS Solut. 28, 85.
Yang, M., Gao, S., Zhong, Y., Hu, G., Subic, A., 2016. Covariance matching based adaptive unscented Kalman filter for direct filtering in INS/GNSS integration. Acta Astronaut. 120, 171–181.
Zhang, J., Chen, D., Wang, S.M., 2015. Research of INS/GNSS heading information fusion method for agriculture machinery automatic navigation system. Trans. Chin. Soc. Agric. Mach. 46, 1–7 in Chinese.
Zhang, X., Zhu, F., Tao, X., et al., 2017. New optimal smoothing scheme for improving relative and absolute accuracy of tightly coupled GNSS/SINS integration. GPS Solut. 21, 861–872.
Zhang, J., Gao, S., Zhong, Y., Qi, X., Xia, J., Yang, J., 2019. An advanced cubature information filtering for indoor multiple wideband source tracking with a distributed noise statistics estimator. IEEE Access 7, 151851–151866.
Zhang, Q., Chen, Q., Xu, Z., et al., 2021. Evaluating the navigation performance of multi-information integration based on low-end inertial sensors for precision agriculture. Precis. Agric. 22, 627–646.
Zhou, X.L., Xu, X.C., Zhang, J.F., Wang, L., Wang, D.F., Zhang, P.P., 2023. Fault diagnosis of silage harvester based on a modified random forest. Inf. Process. Agric. 10 (3), 301–311.